



# Reaction Pathways and Energy Consumption in $\text{NH}_3$ Decomposition for $\text{H}_2$ Production by Low Temperature, Atmospheric Pressure Plasma

Brian N. Bayer<sup>1</sup> · Aditya Bhan<sup>1</sup> · Peter J. Bruggeman<sup>2</sup>

Received: 27 July 2024 / Accepted: 16 August 2024

© The Author(s), under exclusive licence to Springer Science+Business Media, LLC, part of Springer Nature 2024

## Abstract

Pathways for  $\text{NH}_3$  decomposition to  $\text{N}_2$  and  $\text{N}_2\text{H}_4$  by atmospheric pressure nonthermal plasma are analyzed using a combination of molecular beam mass spectrometry measurements and zero-dimensional kinetic modeling. Experimental measurements show that  $\text{NH}_3$  conversion and selectivity towards  $\text{N}_2$  formation scale monotonically with the specific energy input into the plasma with  $\sim 100\%$  selectivity to  $\text{N}_2$  formation achieved at specific energy inputs above  $0.12 \text{ J cm}^{-3}$  ( $3.1 \text{ eV (molecule NH}_3\text{)}^{-1}$ ). The kinetic model recovers these trends, although it underpredicts  $\text{N}_2$  selectivity at low specific energy input. These discrepancies can be explained by the underestimation of reaction rate coefficients for reactions that consume  $\text{N}_2\text{H}_x$  species in collisions with H radicals and/or radial nonuniformities in power deposition, gas temperature, and species concentrations that are not represented by the plug flow approximation used in the model. The kinetic model shows that  $\text{N}_2$  formation proceeds through  $\text{N}_2\text{H}_x$  decomposition pathways rather than  $\text{NH}_x$  decomposition pathways in low temperature, atmospheric pressure plasma. Higher selectivity toward  $\text{N}_2$  production can be achieved by operating at higher  $\text{NH}_3$  conversion and with a higher gas temperature. The high energy cost of  $\text{NH}_3$  decomposition by atmospheric pressure nonthermal plasma found in this work ( $25\text{--}50 \text{ eV (molecule NH}_3\text{ converted)}^{-1}$ ;  $17\text{--}33 \text{ eV (molecule H}_2\text{ formed)}^{-1}$ ) is a result of the energy requirement for electron-impact dissociation of  $\text{NH}_3$  and the significant re-formation of  $\text{NH}_3$  by three-body recombination reactions between  $\text{NH}_2$  and H.

**Keywords** Nonthermal plasma · Ammonia decomposition · Molecular beam mass spectrometry · Kinetic modeling

---

✉ Aditya Bhan  
abhan@umn.edu

✉ Peter J. Bruggeman  
pbruggem@umn.edu

<sup>1</sup> Department of Chemical Engineering and Materials Science, University of Minnesota-Twin Cities, 421 Washington Ave. SE, Minneapolis, MN 55455, USA

<sup>2</sup> Department of Mechanical Engineering, University of Minnesota-Twin Cities, 111 Church St. SE, Minneapolis, MN 55455, USA

## Introduction

$\text{NH}_3$  can potentially serve as a platform molecule to store renewable energy in a medium that can be easily stored and transported [1]. However, before energy conversion by combustion or in fuel cells,  $\text{NH}_3$  must be partially or fully decomposed into  $\text{N}_2$  and  $\text{H}_2$  because  $\text{NH}_3$  has a low flammability, is difficult to ignite, and  $\text{NH}_3$  fuel cell technology is less developed than  $\text{H}_2$  fuel cell technology [2].  $\text{NH}_3$  decomposition to  $\text{N}_2$  and  $\text{H}_2$  is an endothermic reaction with a positive entropy of reaction ( $\Delta H=46 \text{ kJ (mol NH}_3\text{)}^{-1}=0.48 \text{ eV (molecule NH}_3\text{)}^{-1}$ ;  $\Delta S=99 \text{ J (mol NH}_3\text{)}^{-1} \text{ K}^{-1}$ ) [3]. To operate at process conditions that favor  $\text{NH}_3$  decomposition, gas-phase  $\text{NH}_3$  pyrolysis typically occurs at temperatures above 1000 K [4]. Heterogeneous catalysts can be utilized to lower operating temperatures for  $\text{NH}_3$  decomposition to  $\sim 700 \text{ K}$ ; however, currently the most effective catalysts are expensive noble metals (Ru) [5].  $\text{NH}_3$  decomposition can be carried out catalytically at lower temperatures by oxidative reforming processes, although this method sacrifices some  $\text{H}_2$  to form  $\text{H}_2\text{O}$  to make the overall reaction more exothermic [5].

Nonthermal plasma provides an opportunity to drive  $\text{NH}_3$  decomposition at low temperatures utilizing high-energy electrons to excite or dissociate N–H bonds in  $\text{NH}_3$ . Qiu et al. [6], Gao et al. [7], and Ruiz-Martín et al. [8] demonstrate that atmospheric pressure, nonthermal plasma can drive  $\text{NH}_3$  decomposition in Ar/ $\text{NH}_3$  or pure  $\text{NH}_3$  discharges without external heating, indicating that the plasma can drive  $\text{NH}_3$  decomposition via nonthermal processes or in-situ heating. Kinetic models to describe  $\text{NH}_3$  decomposition in Ar/ $\text{NH}_3$  microdischarges at 100 torr developed by Arakoni et al. [9] show that  $>95\%$  of  $\text{NH}_3$  dissociation is induced by electron impact processes at select process conditions, indicating that  $\text{NH}_3$  decomposition can be driven by nonthermal processes. They also investigated how changing operating conditions can optimize the energy cost of  $\text{H}_2$  production, noting an optimal energy cost of  $\text{H}_2$  production equal to  $3.3 \text{ eV (molecule H}_2\text{ consumed)}^{-1}$ . They, as well as Qiu et al. [6], note that this energy cost is higher than the heat of combustion of  $\text{H}_2$  ( $-2.5 \text{ eV (molecule H}_2\text{ consumed)}^{-1}$  [3]), which is the amount of energy that can be recovered from  $\text{H}_2$  oxidation in a fuel cell. These studies do not, however, analyze the chemical or physical processes that dictate the energy cost in order to identify methods to lower the energy cost of the plasma-driven  $\text{NH}_3$  decomposition.

$\text{N}_2$  and  $\text{H}_2$  are not the only products that can form from  $\text{NH}_3$  decomposition. Fateev et al. [10] note that  $\text{N}_2\text{H}_4$  (hydrazine), a toxic compound and a strong reductant [11], was a side product of  $\text{NH}_3$  decomposition in an Ar/ $\text{NH}_3$  DBD at 300 K. They posit that  $\text{N}_2\text{H}_4$  was formed from three-body collisions between  $\text{NH}_2$  radicals but do not perform extensive experiments or kinetic modeling to validate this claim. Bang et al. [12] investigated possible mechanisms for  $\text{NH}_3$  decomposition in a 1%  $\text{NH}_3$  / 99%  $\text{N}_2$  atmospheric pressure dielectric barrier discharge using a combination of experimental measurements and kinetic modeling. According to their proposed reaction mechanism,  $\text{N}_2\text{H}_4$  is formed from three-body collisions between  $\text{NH}_2$  radicals, although they do not measure  $\text{N}_2\text{H}_4$  in their experiments to help validate their proposed reaction pathways. Their mechanism shows that  $\text{N}_2\text{H}_4$  may be an intermediate in  $\text{NH}_3$  decomposition but that  $\text{NH}_3$  decomposition can also proceed through  $\text{NH}_x$  decomposition pathways mediated by the presence of  $\text{N}_2$ -derived species in their plasma.

This work utilizes a combination of molecular beam mass spectrometry and zero-dimensional kinetic modeling to assess energy consumption and reaction pathways involved in  $\text{NH}_3$  decomposition and formation of  $\text{N}_2$  and  $\text{N}_2\text{H}_4$  in an RF-driven atmospheric pressure plasma jet. Experimental measurements show that  $\text{NH}_3$  conversion and selectivity towards

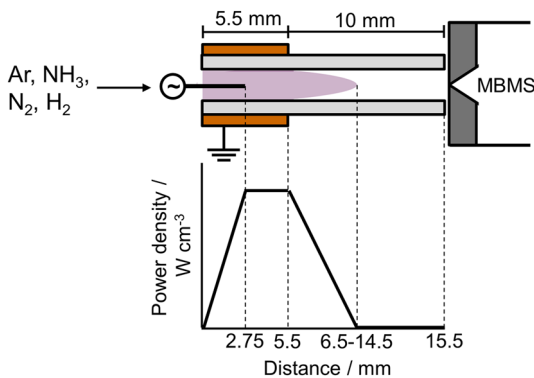
$N_2$  formation increases with the specific energy input into the system. Kinetic modeling results recover these trends but underpredict selectivity toward  $N_2$ . These underpredictions can be resolved by considering potential inaccuracies associated with reaction rate constants and/or radial nonuniformities in power deposition, gas temperature, and species concentrations that cannot be described with a plug-flow approximation. Results of the kinetic model demonstrate that  $N_2H_4$  is an intermediate in  $N_2$  formation from  $NH_3$  decomposition at atmospheric pressure.  $N_2H_4$  production can be mitigated by operating the plasma jet at higher  $NH_3$  conversion and higher gas temperature. The kinetic model demonstrates that  $NH_3$  dissociation is induced by electron impact dissociation, which has an energy threshold of 5.72 eV [13]. This gives a lower bound on energy cost for  $H_2$  production to be  $3.8 \text{ eV (molecule } H_2 \text{ produced)}^{-1}$  if electron impact dissociation is the dominant method of  $NH_3$  dissociation. This value is higher than the heat of combustion of  $H_2$ , indicating that plasma-driven  $NH_3$  decomposition via solely electron impact dissociation processes would cost too much energy to be utilized to produce  $H_2$  for energy storage applications. Recombination reactions between  $NH_2$  and  $H$  to form  $NH_3$  further increase the energy cost of low temperature plasma-driven  $NH_3$  decomposition at atmospheric pressure.

## Methods

### Plasma Jet and MBMS Setup

An RF-driven (13.8 MHz) atmospheric pressure plasma jet with a feed gas containing mixtures of 5%  $NH_3$  in Ar (Airgas),  $N_2$  (HP, Airgas, 99.998% purity), 4%  $H_2$  in Ar (HP, Airgas, 99.995% purity), and Ar (UPC, Airgas, 99.9993% purity) at total flow rates ranging from 0.5 to 6.0 standard liters per minute (slm) was utilized in this work (Fig. 1). The jet consisted of a 3 mm outer diameter, 2 mm inner diameter quartz tube with two electrodes: an inner 1 mm diameter tungsten needle electrode and an outer copper ring electrode (5.5 mm long), with the tip of the needle in the center of the ground electrode [14]. The distance between the end of the ground electrode and the nozzle of the plasma jet was kept at 10 mm throughout this work. The sampling plate of the mass spectrometer was placed adjacent to the nozzle ( $<0.2 \text{ mm}$ ). Methods used for the RF power measurement are described in more detail by Hofmann et al. [15]. The plasma-on power was varied from 2.2 to 4.05 W in this work, with an optional 20 kHz, 50% duty cycle modulation utilized to lower the average

**Fig. 1** Experimental setup and power density profile utilized in the kinetic model



power by a factor of two. The waveform was modulated with an additional 10 Hz modulation cycle to enable multi-channel scaler measurements with the MBMS (Sect. “Molecular Beam Mass Spectrometry (MBMS) Methods”).

## Molecular Beam Mass Spectrometry (MBMS) Methods

MBMS was utilized in this work to detect and quantify densities of  $N_2$ ,  $H_2$ ,  $NH_3$ , and  $N_2H_4$ . Details about the setup and operation of the MBMS are described in more detail in previous work [16, 17]. Table 1 displays the MBMS methods used in this work to detect and quantify these species.  $NH_3$  was detected at an electron energy of 16 eV to reduce the background signal coming from the dissociative ionization of  $H_2O$  ( $m_{NH_3^+} = m_{OH^+} = 17$ ) in the last stage of the MBMS, and  $N_2H_4$  was detected at an electron energy of 15 eV to potentially reduce the background signal coming from the ionization of  $O_2$  ( $m_{N_2H_4^+} = m_{O_2^+} = 32$ ) in the last stage of the MBMS.  $N_2$  was utilized to calibrate  $N_2H_4$  densities due to their similar mass [18]. An additional correction was made when calibrating for  $N_2H_4$  to account for the differences in ionization cross sections between  $N_2$  and  $N_2H_4$  [19]. Attempts to measure the densities of N, H, NH,  $NH_2$ ,  $N_2H$ ,  $N_2H_2/H_2NN$ , and  $N_2H_3$  were also pursued using methods described in previous work [17]. Densities of these species, aside from possibly  $N_2H_3$ , were below the detection limit ( $\sim 10^{13}$ – $10^{14}$   $cm^{-3}$  for N,  $NH_x$ , and  $N_2H_x$ ;  $\sim 10^{15}$   $cm^{-3}$  for H) for the investigated operating conditions [17]. A signal for  $N_2H_3$  ( $m/z = 31$  at 15 eV) could be detected but was consistently smaller than the  $N_2H_4$  signal. It is possible that this signal could arise from dissociative ionization of  $N_2H_4$  in the ionizer of the mass spectrometer, so the detection and enumeration of this species was not investigated in detail in this work.

A multichannel scaler measurement with a plasma modulation at 10 Hz was utilized to quantify changes in the MBMS signal when the plasma was on and off, which can occur due to chemical reactions that consume/form species, vibrational excitation (for  $N_2$ ) [20, 21], or gas heating if the species is present in the feed gas [22]. For Ar/ $NH_3$  plasmas,  $H_2$  formation ( $\Delta c_{H_2}$ ) and  $N_2H_4$  formation ( $\Delta c_{N_2H_4}$ ) were quantified, and  $NH_3$  consumption ( $\Delta c_{NH_3}$ ) and  $N_2$  formation ( $\Delta c_{N_2}$ ) due to chemical reactions were calculated using H- (Eq. 1) and N- (Eq. 2) atom balances, assuming that  $N_2$ ,  $H_2$ , and  $N_2H_4$  were the only products formed:

$$\Delta c_{NH_3} = -\left(\frac{2}{3}\Delta c_{H_2} + \frac{4}{3}\Delta c_{N_2H_4}\right) \quad (1)$$

$$\Delta c_{NH_3} = -2(\Delta c_{N_2} + \Delta c_{N_2H_4}) \quad (2)$$

This method eliminates confounding effects that gas heating may have on the  $NH_3$  signal and that vibrational excitation may have on the  $N_2$  signal.

**Table 1** Summary of detection and calibration methods used for species of interest in this work

Species	m/z	Electron energy / eV	Calibration gas
$NH_3$	17	16	$NH_3$
$H_2$	2	70	$H_2$
$N_2$	28	70	$N_2$
$N_2H_4$	32	15	$N_2$

$\text{NH}_3$  fractional conversion ( $X_{\text{NH}_3}$ ) and  $\text{N}_2$  selectivity ( $S_{\text{N}_2}$ ) are computed to compare results between experiments and simulations among different process conditions.  $\text{NH}_3$  fractional conversion is calculated using Eq. 3:

$$X_{\text{NH}_3} = \frac{-\Delta c_{\text{NH}_3}}{c_{\text{NH}_3, \text{inlet}} \frac{T_{g, \text{out}}}{300\text{K}}} \quad (3)$$

In Eq. 3,  $c_{\text{NH}_3, \text{inlet}}$  is the concentration of  $\text{NH}_3$  at the inlet of the reactor, and  $T_{g, \text{out}}$  is the gas temperature at the outlet. The  $\frac{T_{g, \text{out}}}{300\text{K}}$  term in Eq. 3 accounts for the decrease in the inlet concentration of  $\text{NH}_3$  due to gas heating.  $T_{g, \text{out}}$  is calculated using Eq. 7 described in Sect. “Zdplaskin Model”.  $\text{N}_2$  selectivity is calculated using Eq. 4, assuming that  $\text{N}_2$  and  $\text{N}_2\text{H}_4$  are the most abundant nitrogen-containing products of  $\text{NH}_3$  decomposition:

$$S_{\text{N}_2} [\%] = \frac{\Delta c_{\text{N}_2}}{\Delta c_{\text{N}_2} + \Delta c_{\text{N}_2\text{H}_4}} \cdot 100 \quad (4)$$

## Zdplaskin Model

A kinetic model was developed using *zdplaskin* to determine the important pathways and reactions relevant to  $\text{NH}_3$  decomposition in the experiments. *Zdplaskin* [23] concurrently solves species concentration balances, the energy balance for heavy species, and the Boltzmann equation for the electron energy distribution using Bolsig [24]. Electron–electron and electron–ion collisions were not considered when using Bolsig due to the low degree of ionization ( $< 10^{-7}$ ). The inlet gas composition, gas flow rate, inlet gas temperature, pressure, and power deposition profile were used as inputs for the model. A finite but small seed electron density ( $10^7 \text{ cm}^{-3}$ ) and reduced electric field (0.001 Td) were used as inlet conditions to initiate the simulations.

The power density profile used in simulations is displayed in Fig. 1 and was assumed to rise from the start of ground electrode to the end of the inner electrode, stay constant from the end of the inner electrode to the end of the ground electrode, and fall from the end of the ground electrode to the end of the plasma plume, which depends on the experimental operating condition (Table S6). Integration of the power density profile over the volume of the reactor yields the experimentally measured power at the corresponding operating condition. For experiments that utilized 20 kHz modulation with a 50% duty cycle, corresponding simulations did not employ power modulation but rather operated with continuous power deposition decreased by a factor of two. This method has been demonstrated to reasonably approximate the effects of power modulation [25]. Power density ( $P_{\text{dens}}$ ) was converted to reduced electric field ( $E/N$ ; electric field divided by gas density), the input required for *zdplaskin*, at each timestep using Eq. 5 and Eq. 6:

$$P_{\text{dens}} = JE \quad (5)$$

$$J = n_e v_{\text{drift}} \quad (6)$$

In Eq. 5 and Eq. 6,  $J$  is the current density,  $E$  is the electric field strength,  $n_e$  is the electron density, and  $v_{\text{drift}}$  is the electron drift velocity. *Zdplaskin* calculates the current density by calculating the electron density and drift velocity iteratively at each timestep in the plasma. The model assumes an effective DC electric field in contrast to the RF

field used in experiments. Gas heating due to power deposition was considered in the model using Eq. 7:

$$T_g(\tau) = 300 + \int_0^\tau \frac{RT_g(t)}{pC_{p,Ar}} P_{dens}(t) dt \quad (7)$$

In Eq. 7,  $\tau$  is the residence time in the reactor,  $R$  is the gas constant,  $p$  is the gas pressure ( $10^5$  Pa),  $C_{p,Ar}$  is the heat capacity of Ar at constant pressure [ $\text{J mol}^{-1} \text{K}^{-1}$ ], and  $t$  is time. This method provides an upper bound on the gas temperature increase through the reactor but is a reasonable estimate because only a small fraction of the energy deposited into the plasma goes into changing the end chemical composition of the system (see Sect. “[Assessment of the Energy Efficiency of Plasma-Driven  \$\text{NH}\_3\$  Decomposition](#)”). and because gas residence times are short ( $< 5$  ms) so that radial heat transfer away from the plasma jet is insignificant [26]. Outlet gas temperatures are listed in Table S6 for each simulation and range from 313 to 617 K.

Time, the independent variable in `zdpplaskin`, was converted to distance ( $z$ ) using Eq. 8 by considering the inlet volumetric flow rate ( $F$ ), the cross sectional area of the reactor ( $A$ ), and changes in the volumetric gas flow rate due to gas heating.

$$z(\tau) = \int_0^\tau \frac{F}{A(t)} \frac{T_g(t)}{300 \text{ K}} dt \quad (8)$$

The change in volumetric flow rate that would occur due to molar expansion (an increase in molecules due to the stoichiometry of  $\text{NH}_3$  decomposition) was neglected due to the high degree of dilution used in this work (99% Ar).

The source code for the reaction set was developed using the reaction set made available by Bang et al. [12]. The reaction set was modified to include reactions involving Ar-derived species and by replacing rate coefficients that were potentially inaccurate. A detailed list of reactions and their rate constants is presented in the supporting information (section S.1.). Electron-impact reactions involving  $\text{NH}_3$  and Ar were taken from the Hayashi database, and electron-impact reactions involving  $\text{N}_2$  and  $\text{H}_2$  were taken from the Lisbon database [13, 27]. Vibrational excitation of  $\text{N}_2$ ,  $\text{H}_2$ , and  $\text{NH}_3$  by electron impact was considered in the model for purposes of determining the electron energy distribution function (EEDF), although concentrations of the vibrationally excited states of these species were assumed to remain at zero in the model. Electron impact reactions involving  $\text{NH}_2$ ,  $\text{NH}$ ,  $\text{N}$ , and  $\text{H}$  were not considered because the addition of these reactions caused segmentation faults when trying to run `zdpplaskin`. It is assumed that the inclusion of these reactions would not significantly change the EEDF or concentrations of these species because they accumulate to densities that are smaller than the densities of Ar,  $\text{N}_2$ ,  $\text{H}_2$ , and  $\text{NH}_3$ . Reaction rate coefficients for ion recombination reactions, charge transfer reactions, and chemistry related to Ar- and N-based excited states were taken from Bang et al. [12], Arakoni et al. [9], and Van Gaens & Bogaerts [28]. Reaction rate coefficients involving ground state neutral species were mostly taken from the  $\text{NH}_3$  pyrolysis mechanism from Alturaifi et al. [29]. As noted by Bang et al. [12], some of the reaction rate coefficients for three-body recombination reactions presented by Alturaifi et al. [29] extrapolate to unrealistic values near 300 K. For these reactions, rate constants were taken from alternative sources [30–33]. Reaction rate coefficients for the reverse reactions of those listed by Alturaifi et al. [29] and alternative sources [30–33] were calculated using the principle of detailed balance with thermodynamic data from

the NIST database [3] for all species aside from  $N_2H_x$  species. For  $N_2H_x$  species, thermodynamic data was retrieved from the Burcat database [34].

## Results

MBMS measurements were performed to assess the influence that power and flow rate have on  $NH_3$  conversion and formation of  $N_2$  and  $N_2H_4$  for 1%  $NH_3$  in Ar plasma (Figure S1). These data were reformulated to plot  $NH_3$  consumption and selectivity towards  $N_2$  formation as a function of specific energy input (SEI, the power divided by the flow rate) as shown in Fig. 2. This figure shows that  $NH_3$  conversion and  $N_2$  selectivity (with  $N_2H_4$  being the other N-containing product) monotonically increase with SEI. The observation that  $NH_3$  fractional conversion increases with SEI is consistent with previous studies of plasma-driven  $NH_3$  decomposition [9].

Increasing the SEI will increase both the electron density and the gas temperature of the plasma. Therefore, the increase in  $NH_3$  fractional conversion and  $N_2$  selectivity with higher SEI can result from nonthermal (electron-driven) and/or thermal (temperature-driven) processes. The correlation between the higher selectivity toward  $N_2H_4$  formation at lower  $NH_3$  conversions also suggests that  $N_2H_4$  could be a primary product of  $NH_3$  decomposition that then reacts further to form  $N_2$ . Measurements were made to compare  $N_2H_4$  production in Ar/ $NH_3$  plasma and Ar/ $N_2/H_2$  plasma with the same N- and H- content and operating conditions to determine whether  $N_2H_4$  is a product of  $NH_3$  decomposition or is formed from reactions involving plasma-derived  $N_2/H_2$  species (Fig. 3(a)).  $N_2H_4$  formation is measurable in Ar/ $NH_3$  plasma, whereas  $N_2H_4$  formation is below the detection limit in Ar/ $N_2/H_2$  plasma, indicating that  $N_2H_4$  is indeed a product of  $NH_3$  decomposition rather than reactions involving plasma-derived  $N_2/H_2$  species. These data also show that the plasma jet induces a greater change in  $NH_3$  density in Ar/ $NH_3$  plasma than in Ar/ $N_2/H_2$  plasma by  $>20\times$  (Fig. 3(b)). This observation demonstrates that at these investigated operating conditions, the atmospheric pressure RF plasma jet more effectively channels energy towards reactions that decompose  $NH_3$  than reactions that synthesize  $NH_3$ .

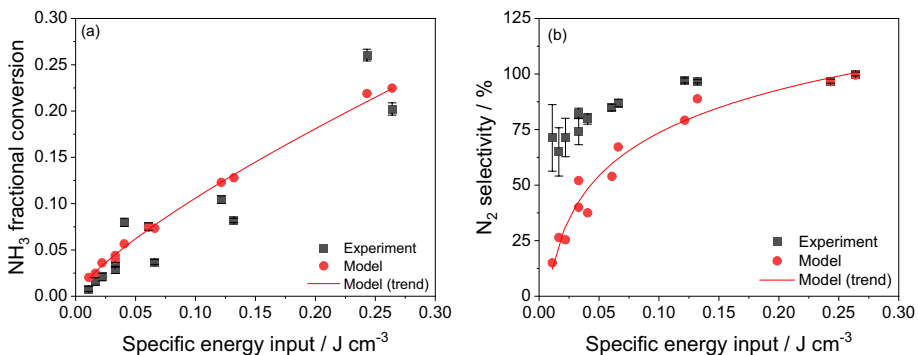


**Fig. 2** A comparison between SEI and **a**  $NH_3$  fractional conversion and **b**  $N_2$  selectivity measured in experiments and predicted by kinetic modeling simulations. Experimental conditions: 1%  $NH_3$  in Ar, 0.5–6 slm, 13.8 MHz, 2.2–4.05 W plasma-on power, 10 Hz, 50% duty cycle modulation for MBMS measurements. For the 1.1 W data, the plasma was run with 2.2 W plasma-on power with 20 kHz, 50% duty cycle modulation. Error bars represent 95% confidence intervals.  $1 \text{ J cm}^{-3} = 26 \text{ eV (NH}_3 \text{ molecule)}^{-1}$ . The lines in **a** and **b** serve as a guide to the eye to describe the trend of the kinetic modeling simulation results

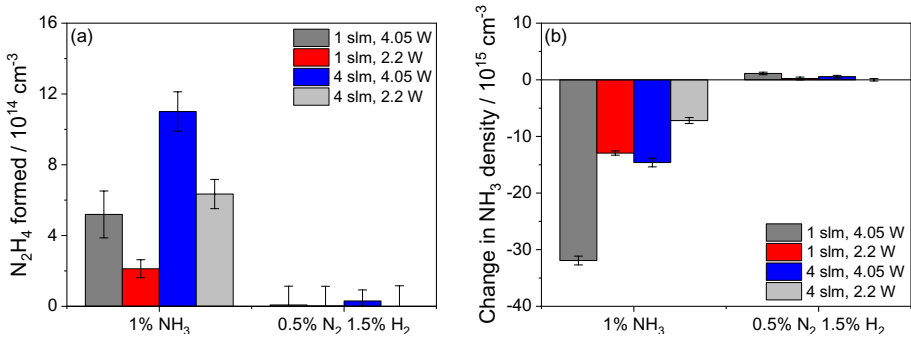


**Fig. 3** **a**  $N_2H_4$  formation and **b** changes in  $NH_3$  density in 1%  $NH_3$  in Ar and 0.5%  $N_2$ , 1.5%  $H_2$  in Ar plasma. Experimental conditions: 1%  $NH_3$  in Ar, 1–4 slm, 13.8 MHz, 2.2–4.05 W plasma-on power, 10 Hz, 50% duty cycle modulation for MBMS measurements. Error bars represent 95% confidence intervals

To determine which reactions contribute to  $NH_3$  decomposition,  $N_2H_4$  production, and  $N_2$  production, kinetic modeling was performed with the model described in Sect. “Zdplaskin Model”, to simulate the process conditions reported in Fig. 2. The results from these simulations are plotted in Fig. 2 alongside the experimental data. The simulations quantitatively agree with the experimental data relating SEI to  $NH_3$  conversion. Though the simulations systematically underestimate  $N_2$  selectivity, especially at lower SEI, they do accurately reproduce the observation that  $N_2$  selectivity increases with SEI.

Axial changes in concentrations of intermediates and reaction rates predicted by the model are analyzed to assess reaction pathways and chemical reactions relevant for  $NH_3$  decomposition and  $N_2/N_2H_4$  formation. Axial variations in power density deposition (as the input, see Sect. “Zdplaskin Model”), electron density, electron temperature, gas temperature, and concentrations of products ( $N_2H_4$ ,  $N_2$ ,  $H_2$ ) and intermediates ( $N$ ,  $H$ ,  $NH$ ,  $NH_2$ ,  $N_2H$ ,  $N_2H_2$ ,  $H_2NN$ ,  $N_2H_3$ ) are displayed in Fig. 4. The electron density is proportional to the power deposition profile in the plasma and then decays in the afterglow. The electron temperature in the plasma predicted by the model ( $\sim 2$  eV) is slightly higher and the electron density ( $\sim 10^{11}$  cm<sup>-3</sup>) is lower than what would be expected for atmospheric pressure RF plasma jets, which typically have electron temperatures around 1–2 eV and electron densities  $\sim 10^{12}$ – $10^{13}$  cm<sup>-3</sup> [15, 35, 36]. This has been previously observed in global models that spatially average plasma parameters and is ascribed to not considering secondary emission from metal electrodes or photoionization as ionization sources in such models [25, 37].

Species density profiles shown in Fig. 4(b) demonstrate that  $N_2H_4$  density peaks in the plasma at around 0.44 cm (650  $\mu$ s) and then decays simultaneously with a rise in  $N_2$  density, suggesting that  $N_2H_4$  forms over shorter timescales in the plasma and then is consumed to form  $N_2$  over longer timescales. The decrease in  $NH_3$  density exhibited in Fig. 4(b) mostly occurs due to gas rarefaction, since the gas temperature increases from 300 to 448 K due to gas heating (Fig. 4(a)). The data in Fig. 4(c) show that concentrations of  $N_2H_x$  species decrease as the degree of hydrogenation decreases, indicating that these species become more unstable as more hydrogen is removed. Axial profiles of  $NH_2$  reported in Fig. 4(d) show that  $NH_2$  concentrations are highest in the plasma but then drop by over two orders of magnitude in  $< 100$   $\mu$ s in the spatial afterglow of the plasma because of its high reactivity.



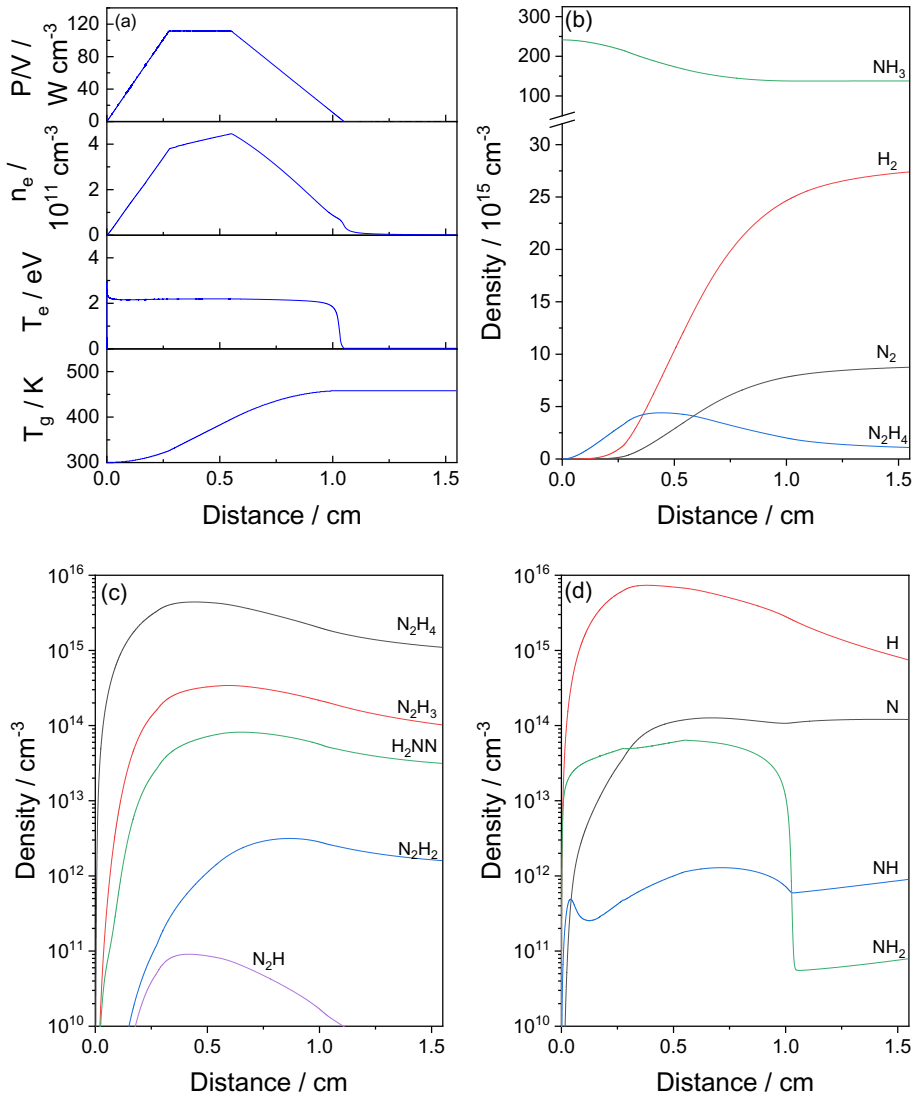


**Fig. 4** Axial profiles of **a** power density, electron density, electron temperature, and gas temperature; **b**  $\text{NH}_3$ ,  $\text{N}_2$ ,  $\text{H}_2$ , and  $\text{N}_2\text{H}_4$  densities; **c**  $\text{N}_2\text{H}_4$ ,  $\text{N}_2\text{H}_3$ ,  $\text{H}_2\text{NN}$ ,  $\text{N}_2\text{H}_2$ , and  $\text{N}_2\text{H}$  densities; and **d** H, N, NH, and  $\text{NH}_2$  densities predicted by the kinetic model for 1%  $\text{NH}_3$  in Ar, 1 slm, 2.2 W. 1 cm of distance corresponds to between 1.2 and 1.8 ms of gas residence time (Figure S3)

Axially resolved rates for formation and consumption of  $\text{NH}_3$ ,  $\text{N}_2\text{H}_4$ , and  $\text{N}_2$  were assessed to identify the reaction steps that contribute most to formation and consumption of these species (Fig. 5). For reactions that do not involve electrons or excited states of atoms/molecules, the net rates ( $r_{\text{net}} = r_{\text{forward}} - r_{\text{reverse}}$ ) are plotted to express the net rates at which the species of interest are formed or consumed.

Figure 5(a) demonstrates that  $\text{NH}_3$  dissociation to form  $\text{NH}_2$  and H is dominated by electron impact, which is consistent with the inferences of Arakoni et al. [9].  $\text{NH}_3$  is

**Fig. 5** Axial profiles of rates of reactions that **a** form and consume  $\text{NH}_3$ , **b** form and consume  $\text{N}_2\text{H}_4$ , **c** form  $\text{N}_2$ , **d** form  $\text{H}_2$ , **e** consume  $\text{NH}_2$ , and **f** consume  $\text{H}$  predicted by the kinetic model for 1%  $\text{NH}_3$  in Ar, 1 slm, 2.2 W. 1 cm of distance corresponds to between 1.2 and 1.8 ms of gas residence time (Figure S3)

re-formed from the three-body recombination reaction involving  $\text{NH}_2$  and  $\text{H}$  at rates that are on the same order of magnitude as electron impact dissociation of  $\text{NH}_3$ , indicating that a large fraction of energy deposited into dissociation of  $\text{NH}_3$  is wasted to re-form  $\text{NH}_3$ .

Figure 5(b) shows that  $\text{N}_2\text{H}_4$  is mainly formed from the three-body recombination reaction involving  $\text{NH}_2$  radicals in the plasma and through  $\text{N}_2\text{H}_3$  disproportionation reactions in the afterglow.  $\text{N}_2\text{H}_4$  consumption is dominated by  $\text{H}$  abstraction reactions in and after the plasma. Figure 5(c) shows that the dominant pathway for  $\text{N}_2$  formation is through collision-mediated dissociation of  $\text{N}_2\text{H}$ .  $\text{N}_2\text{H}$  is formed from successive dehydrogenation of  $\text{N}_2\text{H}_4$ ,  $\text{N}_2\text{H}_3$ , and  $\text{N}_2\text{H}_2/\text{H}_2\text{NN}$ .  $\text{N}_2$  formation from  $\text{NH}_2 + \text{N}$  occurs at a rate over an order of magnitude lower than  $\text{N}_2$  formation from  $\text{N}_2\text{H}$ , indicating that  $\text{N}_2$  formation mostly occurs through  $\text{N}_2\text{H}_x$  dehydrogenation pathways rather than solely  $\text{NH}_x$  dehydrogenation pathways. Simulations that eliminate reactions that form/consume  $\text{N}_2\text{H}_x$  species predict  $\text{NH}_3$  conversion approximately an order of magnitude lower than those observed in experiments, affirming that the majority of  $\text{N}_2$  formation occurs from  $\text{N}_2\text{H}_x$  dehydrogenation pathways (Fig. 6).  $\text{N}_2$  consumption occurs primarily by dissociative collisions with  $\text{Ar}^*$  species, with maximum rates  $\sim 10^{14} \text{ cm}^{-3} \text{ s}^{-1}$ . Figure 5(d) demonstrates that  $\text{H}_2$  is mostly formed from  $\text{H}$  abstraction from  $\text{N}_2\text{H}_x$  species, demonstrating that the presence of  $\text{N}_2\text{H}_x$  species increases the rate of  $\text{H}_2$  formation.  $\text{H}_2$  consumption occurs mostly by electron-impact dissociation, with maximum rates  $\sim 10^{15} \text{ cm}^{-3} \text{ s}^{-1}$ .

Figure 5(e–f) shows the loss pathways of  $\text{NH}_2$  and  $\text{H}$ , the primary products of  $\text{NH}_3$  dissociation. At short times,  $\text{NH}_2$  mostly reacts to form  $\text{N}_2\text{H}_4$ , but after  $\text{NH}_2$  concentration becomes relatively attenuated in comparison to  $\text{H}$  concentrations over longer ( $> 300 \mu\text{s}$ ) timescales (Fig. 4(d)),  $\text{NH}_2$  reacts with  $\text{H}$  in three-body recombination reactions at faster rates to re-form  $\text{NH}_3$  (Fig. 5(e)). The reaction between  $\text{NH}_2$  and  $\text{H}$  to form  $\text{NH}$  and  $\text{H}_2$  occurs at a rate nearly two orders of magnitude lower than the three-body recombination reaction to re-form  $\text{NH}_3$  from  $\text{NH}_2$  and  $\text{H}$ . Figure 5(f) demonstrates that  $\text{H}$  is consumed by  $\text{NH}_2 + \text{H} + \text{M}$  and  $\text{N}_2\text{H}_x + \text{H}$  reactions at similar rates.

## Discussion

### Possible Sources of Error in the Model

Though the kinetic model can accurately describe  $\text{NH}_3$  conversion in the plasma, it systematically overestimates  $\text{N}_2\text{H}_4$  production relative to  $\text{N}_2$  production. To assess possible sources of error in the model, a sensitivity analysis was performed.

The kinetic model described in Sect. “Zdplaskin Model” does not include electron-impact reactions involving  $\text{N}_2\text{H}_x$  species, since reaction rate constants for these reactions are unknown/not reported [12]. To probe the role that dissociation of  $\text{N}_2\text{H}_x$  species by nonthermal reactions could have on driving  $\text{N}_2\text{H}_x$  decomposition to  $\text{N}_2$ , reactions involving dissociation of  $\text{N}_2\text{H}_x$  species by electron impact or by collision with excited states of Ar were included in simulations. For reactions that break an N–N bond in  $\text{N}_2\text{H}_x$  species, rate constants for  $\text{N}_2$  dissociation were utilized, and for reactions that break an N–H bond in  $\text{N}_2\text{H}_x$  species, rate constants for  $\text{NH}_3$  dissociation were utilized. Results of these

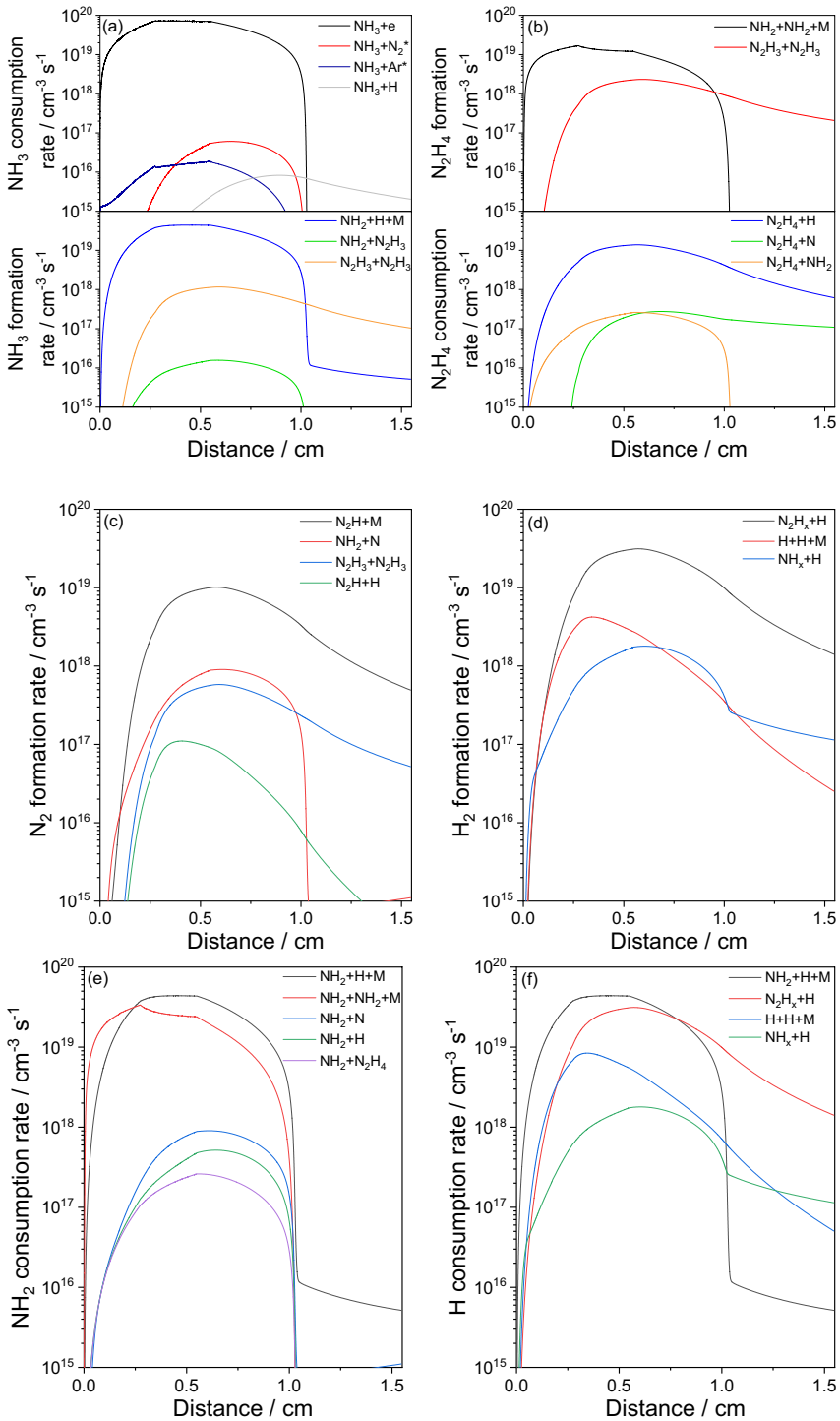
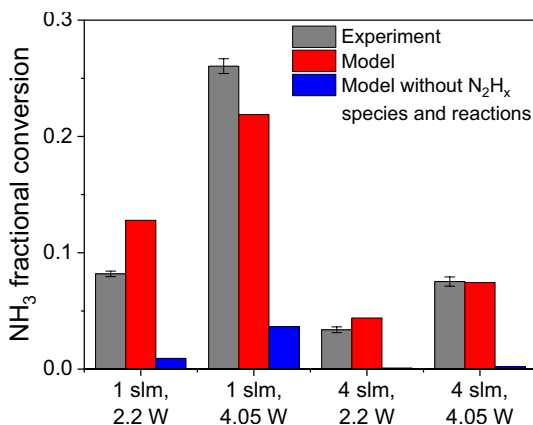


**Fig. 6** A comparison of experimentally measured  $\text{NH}_3$  conversion and  $\text{NH}_3$  conversion predicted by the kinetic model with and without  $\text{N}_2\text{H}_x$  species and reactions. Experimental conditions: 1%  $\text{NH}_3$  in Ar, 1–4 slm, 13.8 MHz, 2.2–4.05 plasma-on power, 10 Hz, 50% duty cycle modulation for MBMS measurements. Error bars represent 95% confidence intervals



simulations show that inclusion of these reactions does result in an increase in  $\text{N}_2$  selectivity but not to the  $\text{N}_2$  selectivity observed in experiments (Fig. 7).  $\text{N}_2$  selectivity is still underpredicted by as much as ~40%.

The kinetic model could also inaccurately predict  $\text{N}_2$  selectivity if the rate coefficients used in the model are inaccurate. A sensitivity analysis was performed in which rate constants for  $\text{N}_2\text{H}_x + \text{H}$  reactions (and their associated reverse reactions) were increased by a factor of four (Fig. 8). Results of these simulations show that the model now predicts  $\text{N}_2$  selectivity accurately within 7%, although the model now systematically overpredicts  $\text{NH}_3$  conversion. These results demonstrate that H abstraction reactions could occur at faster rates than those reported in the model.

Assumptions associated with the plug flow approximation may also contribute to some of the inaccuracies of the simulation results. The model appears to underestimate the electron density and overestimate the electron temperature for reasons discussed in the results section. The plug flow model also assumes that the electron density, electron temperature, gas temperature, and species concentrations are radially uniform at every axial position of the reactor. In the experiments, it is possible that the plasma is constricted, resulting

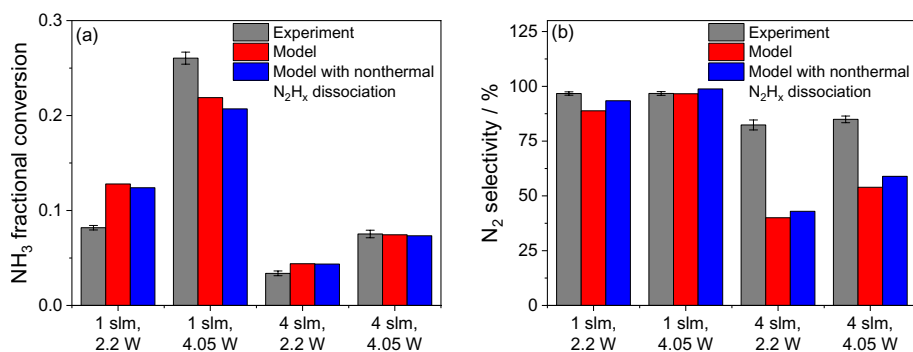


**Fig. 7** A comparison of **a** experimentally measured  $\text{NH}_3$  conversion and  $\text{NH}_3$  conversion predicted by the kinetic model with and without nonthermal  $\text{N}_2\text{H}_x$  dissociation reactions and **b** experimentally measured  $\text{N}_2$  selectivity and  $\text{N}_2$  selectivity predicted by the kinetic model with and without nonthermal  $\text{N}_2\text{H}_x$  dissociation reactions. Experimental conditions: 1%  $\text{NH}_3$  in Ar, 1–4 slm, 13.8 MHz, 2.2–4.05 plasma-on power, 10 Hz, 50% duty cycle modulation for MBMS measurements. Error bars represent 95% confidence intervals

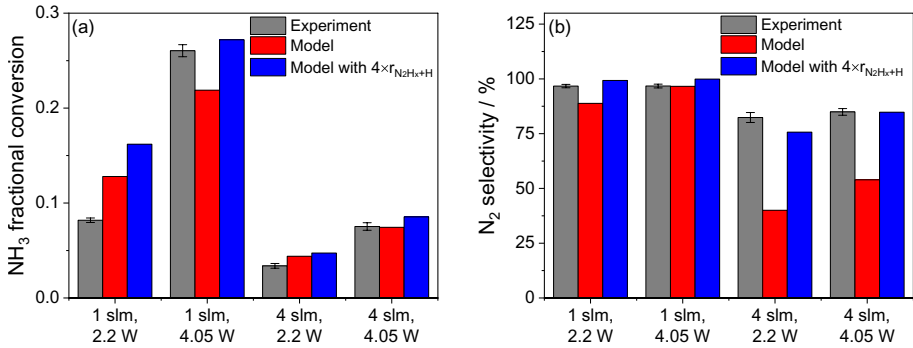


**Fig. 8** A comparison of **a** experimentally measured NH<sub>3</sub> conversion and NH<sub>3</sub> conversion predicted by the kinetic model with and without N<sub>2</sub>H<sub>x</sub>+H reaction rate constants increased 4× and **b** experimentally measured N<sub>2</sub> selectivity and N<sub>2</sub> selectivity predicted by the kinetic model with and without N<sub>2</sub>H<sub>x</sub>+H reaction rate constants increased 4×. Experimental conditions: 1% NH<sub>3</sub> in Ar, 1–4 slm, 13.8 MHz, 2.2–4.05 plasma-on power, 10 Hz, 50% duty cycle modulation for MBMS measurements. Error bars represent 95% confidence intervals

in regions of the plasma with locally higher gas temperatures and electron densities [38]. Simulations were performed to probe the effect that uneven power deposition may have on dictating the N<sub>2</sub> selectivity and NH<sub>3</sub> conversion. In these simulations, 1/3 of the gas stream is exposed to plasma with 3× the experimental power density. This stream was then mixed with 2/3 of the unreacted gas stream at the outlet of the reactor to yield a stream with the same SEI as those in experiments. Results of these simulations show that the model now predicts higher N<sub>2</sub> selectivity, especially for the experiments with 4 slm gas flow rates (Fig. 9). Though these simulations are an oversimplification because they do not capture mixing between fluid elements that are exposed to different degrees of power deposition over the length of the reactor and do not consider a continuous gradient in power deposition over the radial coordinate, these simulations demonstrate that uneven power deposition, not considered in the plug-flow model, could contribute to the low N<sub>2</sub>H<sub>4</sub> selectivity observed in experiments. Locally higher gas temperatures in a constricted plasma lead

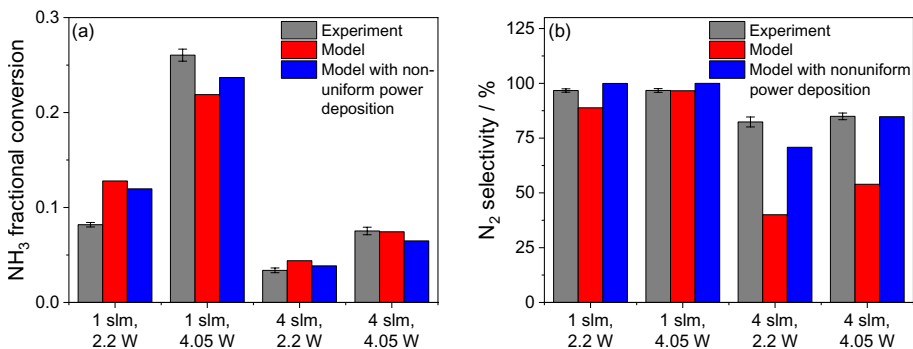


**Fig. 9** A comparison of **a** experimentally measured NH<sub>3</sub> conversion and NH<sub>3</sub> conversion predicted by the kinetic model with and without nonuniform power deposition and **b** experimentally measured N<sub>2</sub> selectivity and N<sub>2</sub> selectivity predicted by the kinetic model with and without nonuniform power deposition. Experimental conditions: 1% NH<sub>3</sub> in Ar, 1–4 slm, 13.8 MHz, 2.2–4.05 plasma-on power, 10 Hz, 50% duty cycle modulation for MBMS measurements. Error bars represent 95% confidence intervals

to a greater extent of  $N_2H_x$  decomposition, since rate constants for  $N_2H_x + H$  reactions increase with gas temperature, while rate constants for the other reactions that consume H ( $NH_2 + H + M$ ,  $H + H + M$ ) are temperature-independent or decrease with temperature (Fig. 5(f), Table S5).

### Assessment of the Energy Efficiency of Plasma-Driven $NH_3$ Decomposition

Experimental data and kinetic modeling results show that  $NH_3$  conversion increases with SEI (Fig. 2(a)). For the 1%  $NH_3$  in Ar plasma investigated in this work, SEI can be converted to energy cost per  $NH_3$  molecule using Eq. 9:

$$\frac{eV}{\text{molecule } NH_3} = 26 \left( \frac{J}{\text{cm}^3} \right) \quad (9)$$

An examination of the slope of the trend in Fig. 2(a) demonstrates  $\sim 25\text{--}50$  eV are required to convert one molecule of  $NH_3$ . This far exceeds the enthalpy of reaction for  $NH_3$  decomposition ( $NH_3 \rightarrow 0.5N_2 + 1.5H_2$ ,  $\Delta H = 46 \text{ kJ (mol } NH_3)^{-1} = 0.48 \text{ eV (} NH_3 \text{ molecule)}^{-1}$ ;  $NH_3 \rightarrow 0.5N_2H_4 + 0.5H_2$ ,  $\Delta H = 94 \text{ kJ (mol } NH_3)^{-1} = 0.97 \text{ eV (} NH_3 \text{ molecule)}^{-1}$ ) [3].

Figure 4(a) demonstrates that electron-impact dissociation is the dominant process driving  $NH_3$  decomposition. The energy threshold for this reaction is 5.72 eV [13], indicating that plasma-driven  $NH_3$  decomposition by electron impact dissociation requires  $10\times$  more energy than the enthalpy of reaction for  $NH_3$  decomposition to form  $N_2$  and  $H_2$  [3]. Therefore, 5.72 eV is the lower bound on energy cost for  $NH_3$  decomposition by nonthermal plasma if electron-impact dissociation is the main reaction driving  $NH_3$  dissociation. This value is equivalent to  $3.8 \text{ eV (molecule } H_2 \text{ produced)}^{-1}$  if  $NH_3$  is decomposed to  $N_2$  and  $H_2$ . As noted by Qiu et al. [6] and Arakoni et al. [9], an energy cost of  $H_2$  production above  $2.5 \text{ eV (molecule } H_2 \text{ produced)}^{-1}$  exceeds the amount of energy that can be recovered from  $H_2$  combustion ( $2.5 \text{ eV (molecule } H_2 \text{ consumed)}^{-1}$ ) [3]. Therefore, plasma-driven  $NH_3$  decomposition solely from electron impact dissociation has an energy cost too high for  $H_2$  production for energy storage purposes. Plasma-driven processes would need to rely on lower energy processes (excitation-driven or thermal-driven) to drive  $NH_3$  decomposition with a suitable energy cost. If the extra dissipated electron energy beyond  $0.48 \text{ eV (} NH_3 \text{ molecule)}^{-1}$  utilized to dissociate  $NH_3$  is effectively utilized to heat the plasma,  $NH_3$  decomposition can be driven by thermal processes in the gas phase [39] or over a catalyst [40, 41].

The  $5.72 \text{ eV (} NH_3 \text{ molecule)}^{-1}$  lower bound is still lower than  $25\text{--}50 \text{ eV (} NH_3 \text{ molecule)}^{-1}$  predicted by experimental measurements and kinetic modeling simulations, so energy dissipation processes are analyzed below to determine where energy is wasted. A comparison between the electron energy deposition into  $NH_3$  dissociation compared to the electron energy deposition into all processes can be analyzed using Eq. 10:

$$\frac{\int_0^{\tau_{end}} E_{NH_3+e} r_{NH_3+e} dt}{\sum_I \int_0^{\tau_{end}} E_{I+e} r_{I+e} dt} \quad (10)$$

In Eq. 10,  $E_{I+e}$  is the energy dissipated in a collision between species I and an electron,  $r_{I+e}$  is the rate at which these collisions occur, and  $\tau_{end}$  is the residence time

associated with the outlet of the reactor (1.55 cm). For the process condition analyzed in Figs. 4–5, this fraction is equal to 0.93, indicating that the plasma very efficiently directs electron energy towards  $\text{NH}_3$  dissociation in comparison to elastic collisions, ionization, excitation, and other dissociation processes.

To assess whether the products of  $\text{NH}_3$  electron impact dissociation are effectively converted to desired products, the fraction of  $\text{NH}_2$  molecules that are converted to  $\text{N}_2\text{H}_4$  vs  $\text{NH}_2$  converted to  $\text{N}_2\text{H}_4$  or  $\text{NH}_3$  can be analyzed using Eq. 11:

$$\frac{\# \text{NH}_2 \text{ to } \text{N}_2\text{H}_4}{\# \text{NH}_2 \text{ converted}} = \frac{\int_0^{\tau_{\text{end}}} 2r_{\text{NH}_2+\text{NH}_2+\text{M}} d\tau}{\int_0^{\tau_{\text{end}}} r_{\text{NH}_2+\text{H}+\text{M}} d\tau + \int_0^{\tau_{\text{end}}} 2r_{\text{NH}_2+\text{NH}_2+\text{M}} d\tau} \quad (11)$$

For the process condition analyzed in Figs. 3 and 4, this fraction is equal to 0.41, indicating that more than half of the  $\text{NH}_2$  molecules formed from electron-impact dissociation of  $\text{NH}_3$  are re-converted to  $\text{NH}_3$ . Limiting the extent to which  $\text{NH}_3$  is re-formed from three-body collisions between  $\text{NH}_2$  and H is critical to improving the utilization of  $\text{NH}_3$  dissociation products for  $\text{N}_2/\text{H}_2$  formation. To do this, process conditions must be chosen that increase the rates at which  $\text{NH}_2$  and H react to form  $\text{N}_2\text{H}_4$  or  $\text{N}_2$  products vs recombine to form  $\text{NH}_3$ . The ratio of the rate of  $\text{N}_2\text{H}_4$  formation vs  $\text{NH}_3$  formation by three-body recombination takes the form of Eq. 12:

$$\frac{r_{\text{NH}_2+\text{NH}_2+\text{M}}}{r_{\text{NH}_2+\text{H}+\text{M}}} = \frac{k_{\text{NH}_2+\text{NH}_2+\text{M}} c_{\text{NH}_2} c_{\text{NH}_2} c_{\text{M}}}{k_{\text{NH}_2+\text{H}+\text{M}} c_{\text{NH}_2} c_{\text{H}} c_{\text{M}}} = \frac{2.1 \cdot 10^{10} c_{\text{NH}_2}}{T_g^{3.41} c_{\text{H}}} \quad (12)$$

An analysis of this ratio shows that the branching ratio between  $\text{N}_2\text{H}_4$  formation and  $\text{NH}_3$  formation is not easily manipulated by varying process conditions. Lower temperature would favor  $\text{N}_2\text{H}_4$  formation over  $\text{NH}_3$  formation, although as the gas temperature increases and  $\text{NH}_2$  concentrations become relatively lower than H concentrations as observed in Fig. 4,  $\text{NH}_2$  consumption to form  $\text{NH}_3$  becomes more pronounced.

Although not a dominant reaction in these experiments, the reaction between  $\text{NH}_2$  and H to form NH and  $\text{H}_2$  can consume  $\text{NH}_2$  and H to eventually form  $\text{N}_2$  and  $\text{H}_2$  instead of re-forming  $\text{NH}_3$ . The ratio of the rates of these processes takes the form of Eq. 13:

$$\frac{r_{\text{NH}_2+\text{H}}}{r_{\text{NH}_2+\text{H}+\text{M}}} = \frac{k_{\text{NH}_2+\text{H}} c_{\text{NH}_2} c_{\text{H}}}{k_{\text{NH}_2+\text{H}+\text{M}} c_{\text{NH}_2} c_{\text{H}} c_{\text{M}}} = \frac{36 \cdot \exp(-1835/T_g) RT_g}{p} \quad (13)$$

This ratio is dependent on both gas temperature and pressure, with higher temperatures and lower pressures favoring  $\text{NH}_2 + \text{H}$  conversion to NH and  $\text{H}_2$  instead of  $\text{NH}_3$ . At atmospheric pressure, 0.1 bar, and 0.01 bar, the ratio of these reaction rates becomes greater than 1 at 1330 K, 630 K, and 386 K, respectively. Operating at lower pressure could thus improve energy efficiency by mitigating re-formation of  $\text{NH}_3$  by three-body recombination reactions involving  $\text{NH}_2$  and H. Additionally, the mechanism for  $\text{N}_2$  formation from  $\text{NH}_3$  decomposition could shift from the  $\text{N}_2\text{H}_x$  formation/decomposition pathway exhibited at atmospheric pressure to a  $\text{NH}_x$  decomposition pathway as rates of three body recombination reactions between two  $\text{NH}_2$  molecules to form  $\text{N}_2\text{H}_4$  become relatively attenuated at reduced pressures. As a result, operating at lower pressure could also improve the selectivity towards  $\text{N}_2$  formation, even at lower temperatures and  $\text{NH}_3$  conversions.

## Conclusions

Reaction pathways and energy consumption for  $\text{NH}_3$  decomposition in an RF-driven atmospheric pressure plasma jet are assessed using a combination of molecular beam mass spectrometry and zero-dimensional kinetic modeling. MBMS measurements show that  $\text{N}_2$  and  $\text{N}_2\text{H}_4$  are the main products of  $\text{NH}_3$  decomposition and that the extent of  $\text{NH}_3$  conversion and the selectivity towards  $\text{N}_2$  formation scales monotonically with the specific energy input into the plasma. Kinetic modeling shows that  $\text{N}_2\text{H}_4$  is an intermediate in  $\text{N}_2$  formation from  $\text{NH}_3$  decomposition and rates of  $\text{N}_2\text{H}_4$  decomposition increase with gas temperature, which explains why  $\text{N}_2\text{H}_4$  selectivity is relatively higher at lower  $\text{NH}_3$  conversion and lower gas temperatures. Though the kinetic model systematically underestimates  $\text{N}_2$  selectivity at low specific energy inputs, a sensitivity analysis demonstrates that this underestimation can be explained by the underestimation of rate constants for reactions that consume  $\text{N}_2\text{H}_x$  species in the model and/or the inaccurate assumption of radially uniform power deposition, gas temperature, and species concentrations associated with the plug-flow approximation of the model.

An analysis of the energy deposition processes shows that  $\text{NH}_3$  dissociation is dominated by electron-impact dissociation in this study, which has an energy threshold of 5.72 eV. Therefore, 5.72 eV is the lower bound on the energy cost for  $\text{NH}_3$  decomposition if electron-impact dissociation is the dominant process for  $\text{NH}_3$  dissociation in plasma. This energy cost is  $\sim 10\times$  higher than the enthalpy of  $\text{NH}_3$  decomposition to  $\text{N}_2$  and  $\text{H}_2$  (0.48 eV (molecule  $\text{NH}_3$  consumed) $^{-1}$ ). This value is also higher than the energy that can be derived from  $\text{H}_2$  combustion (2.5 eV (molecule  $\text{H}_2$  consumed) $^{-1}$ ), indicating that plasma-driven  $\text{NH}_3$  decomposition using electron impact dissociation inherently has an energy cost too high for energy storage applications.  $\text{NH}_3$  re-formation from three-body collisions between  $\text{NH}_2$  and H, the primary products of  $\text{NH}_3$  dissociation, further lowers the energy efficiency of the process. To produce  $\text{H}_2$  from plasma-driven  $\text{NH}_3$  decomposition with an energy cost below 2.5 eV (molecule  $\text{H}_2$  produced) $^{-1}$ , plasma-driven  $\text{NH}_3$  decomposition would need to utilize processes other than electron-impact dissociation to induce  $\text{NH}_3$  dissociation (excitation-driven or thermal-driven) and would need to limit energy loss from  $\text{NH}_3$  re-forming reactions.

**Supplementary Information** The online version contains supplementary material available at <https://doi.org/10.1007/s11090-024-10501-8>.

**Author Contributions** Brian N. Bayer: Conceptualization, Data curation, Formal analysis, Investigation, Methodology, Project administration, Writing—original draft, Writing—review & editing. Aditya Bhan: Conceptualization, Funding acquisition, Methodology, Project administration, Resources, Supervision, Writing—review & editing. Peter J. Bruggeman: Conceptualization, Funding acquisition, Methodology, Project administration, Resources, Supervision, Writing—review & editing.

**Funding** This material is based upon work supported by the U.S. Department of Energy, Office of Science, Office of Fusion Energy Sciences General Plasma Science program under Award Number DE-SC0020232. The work heavily relied on equipment and methods developed within project DE-SC0001939. The authors also acknowledge partial support from the National Science Foundation under Award Number NSF-CBET 2234270.

**Data Availability** All data presented in this work will be made available upon request to the corresponding author.

## Declarations

**Conflict of interest** The authors have no competing interests to declare that are relevant to the content of this article.



## References

1. MacFarlane DR, Cherepanov PV, Choi J, Suryanto BHR, Hodgetts RY, Bakker JM, Ferrero Vallana FM, Simonov AN (2020) A roadmap to the ammonia economy. *Joule* 4:1186–1205. <https://doi.org/10.1016/j.joule.2020.04.004>
2. Valera-Medina A, Xiao H, Owen-Jones M, David WIF, Bowen PJ (2018) Ammonia for power. *Prog Energy Combust Sci* 69:63–102. <https://doi.org/10.1016/j.peccs.2018.07.001>
3. NIST (2010) Standard Reference Database 69: NIST Chemistry WebBook; National Institute of Standards and Technology, (n.d.)
4. Benés M, Pozo G, Abián M, Millera Á, Bilbao R, Alzueta MU (2021) Experimental study of the pyrolysis of  $\text{NH}_3$  under flow reactor conditions. *Energy Fuels* 35:7193–7200. <https://doi.org/10.1021/acs.energyfuels.0c03387>
5. Caballero LC, Thornburg NE, Nigra MM (2022) Catalytic ammonia reforming: alternative routes to net-zero-carbon hydrogen and fuel. *Chem Sci* 13:12945–12956. <https://doi.org/10.1039/D2SC04672E>
6. Qiu H, Martus K, Lee WY, Becker K (2004) Hydrogen generation in a microhollow cathode discharge in high-pressure ammonia–argon gas mixtures. *Int J Mass Spectrom* 233:19–24. <https://doi.org/10.1016/j.ijms.2003.08.017>
7. Gao Y, Zhou M, Hu E, Zhao Y, Yin G, Huang Z (2024) Hydrogen generation by dielectric barrier discharge plasma assisted ammonia decomposition. *Energy Convers Manag* 306:118271. <https://doi.org/10.1016/j.enconman.2024.118271>
8. Ruiz-Martín M, Marín-Meana S, Megías-Sánchez A, Oliva-Ramírez M, Cotrino J, González-Elipe AR, Gómez-Ramírez A (2023)  $\text{H}_2$  Production from  $\text{NH}_3$  in a  $\text{BaTiO}_3$  Moderated ferroelectric packed-bed plasma reactor. *Plasma Chem Plasma Process* 43:2093–2110. <https://doi.org/10.1007/s11090-023-10427-7>
9. Arakoni RA, Bhoj AN, Kushner MJ (2007)  $\text{H}_2$  generation in  $\text{Ar}/\text{NH}_3$  microdischarges. *J Phys D: Appl Phys* 40:2476. <https://doi.org/10.1088/0022-3727/40/8/010>
10. Fateev A, Leipold F, Kusano Y, Stenum B, Tsakadze E, Bindslev H (2005) Plasma chemistry in an atmospheric pressure  $\text{Ar}/\text{NH}_3$  dielectric barrier discharge. *Plasma Process Polym* 2:193–200. <https://doi.org/10.1002/ppap.200400051>
11. Troyan JE (1953) Properties, production, and uses of hydrazine. *Ind Eng Chem* 45:2608–2612. <https://doi.org/10.1021/ie50528a020>
12. Bang S, Snoeckx R, Cha MS (2023) Kinetic study for plasma assisted cracking of  $\text{NH}_3$ : approaches and challenges. *J Phys Chem A* 127:1271–1282. <https://doi.org/10.1021/acs.jpca.2c06919>
13. Hayashi database (2024) (n.d.). [www.lxcat.net](http://www.lxcat.net). Accessed 4 June 2024
14. Kondeti VSSK, Gangal U, Yatom S, Bruggeman PJ (2017)  $\text{Ag}^+$  reduction and silver nanoparticle synthesis at the plasma–liquid interface by an RF driven atmospheric pressure plasma jet: mechanisms and the effect of surfactant. *J Vac Sci Technol, A* 35:061302. <https://doi.org/10.1116/1.4995374>
15. Hofmann S, van Gessel AFH, Verreycken T, Bruggeman P (2011) Power dissipation, gas temperatures and electron densities of cold atmospheric pressure helium and argon RF plasma jets. *Plasma Sources Sci Technol* 20:065010. <https://doi.org/10.1088/0963-0252/20/6/065010>
16. Jiang J, Luo Y, Moldgy A, Aranda Gonzalvo Y, Bruggeman PJ (2020) Absolute spatially and time-resolved  $\text{O}$ ,  $\text{O}_3$ , and air densities in the effluent of a modulated RF-driven atmospheric pressure plasma jet obtained by molecular beam mass spectrometry. *Plasma Process Polym* 17:1900163. <https://doi.org/10.1002/ppap.201900163>
17. Bayer BN, Bruggeman PJ, Bhan A (2023) Species, pathways, and timescales for  $\text{NH}_3$  formation by low-temperature atmospheric pressure plasma catalysis. *ACS Catal* 13:2619–2630. <https://doi.org/10.1021/acscatal.2c05492>
18. Benedikt J, Hecimovic A, Ellerweg D, von Keudell A (2012) Quadrupole mass spectrometry of reactive plasmas. *J Phys D: Appl Phys* 45:403001. <https://doi.org/10.1088/0022-3727/45/40/403001>
19. Singh H, Coburn JW, Graves DB (2000) Appearance potential mass spectrometry: discrimination of dissociative ionization products. *J Vac Sci Technol, A* 18:299–305. <https://doi.org/10.1116/1.582183>
20. Jiang J, Richards C, Adamovich I, Bruggeman PJ (2022) Molecular beam mass spectrometry measurements of vibrationally excited  $\text{N}_2$  in the effluent of an atmospheric plasma jet: a comparison with a state-to-state kinetic model. *Plasma Sources Sci Technol* 31:10LT03. <https://doi.org/10.1088/1361-6595/ac954c>
21. Bayer BN, Raskar S, Adamovich IV, Bruggeman PJ, Bhan A (2023) Availability and reactivity of  $\text{N}_2(\text{v})$  for  $\text{NH}_3$  synthesis by plasma catalysis. *Plasma Sources Sci Technol* 32:125005. <https://doi.org/10.1088/1361-6595/ad10f0>
22. Jiang J, Bruggeman PJ (2021) Tuning plasma parameters to control reactive species fluxes to substrates in the context of plasma catalysis. *J Phys D: Appl Phys* 54:214005. <https://doi.org/10.1088/1361-6463/abc89a>

23. Pancheshni S, Eismann B, Hagelaar GJM, Pitchford LC (2008) Computer code ZDPlasKin. <http://www.zdplaskin.laplace.univ-tlse.fr>
24. Hagelaar GJM, Pitchford LC (2005) Solving the Boltzmann equation to obtain electron transport coefficients and rate coefficients for fluid models. *Plasma Sources Sci Technol* 14:722. <https://doi.org/10.1088/0963-0252/14/4/011>
25. Jiang J, Kondeti VSSK, Nayak G, Bruggeman PJ (2022) Experimental and modeling studies of the plasma chemistry in a humid Ar radiofrequency atmospheric pressure plasma jet. *J Phys D: Appl Phys* 55:225206. <https://doi.org/10.1088/1361-6463/ac570a>
26. Bayer BN, Bruggeman PJ, Bhan A (2024) NO formation by N<sub>2</sub>/O<sub>2</sub> plasma catalysis: the impact of surface reactions, gas-phase reactions, and mass transport. *Chem Eng J* 482:149041. <https://doi.org/10.1016/j.cej.2024.149041>
27. Lisbon database (2024) (n.d.). [www.lxcat.net](http://www.lxcat.net). Accessed 4 June 2024
28. Gaens WV, Bogaerts A (2013) Kinetic modelling for an atmospheric pressure argon plasma jet in humid air. *J Phys D: Appl Phys* 46:275201. <https://doi.org/10.1088/0022-3727/46/27/275201>
29. Alturraifi SA, Mathieu O, Petersen EL (2022) An experimental and modeling study of ammonia pyrolysis. *Combust Flame* 235:111694. <https://doi.org/10.1016/j.combustflame.2021.111694>
30. Gordiets B, Ferreira CM, Pinheiro MJ, Ricard A (1998) Self-consistent kinetic model of low-pressure - flowing discharges: I. volume processes. *Plasma Sources Sci Technol* 7:363–378. <https://doi.org/10.1088/0963-0252/7/3/015>
31. Pagsberg PB, Eriksen J, Christensen HC (1979) Pulse radiolysis of gaseous ammonia-oxygen mixtures. *J Phys Chem* 83:582–590. <https://doi.org/10.1021/j100468a006>
32. Zheng J, Rocha RJ, Pelegrini M, Ferrão LFA, Carvalho EFV, Roberto-Neto O, Machado FBC, Truhlar DG (2012) A product branching ratio controlled by vibrational adiabaticity and variational effects: Kinetics of the H + trans-N<sub>2</sub>H<sub>2</sub> reactions. *J Chem Phys* 136:184310. <https://doi.org/10.1063/1.4707734>
33. Altinay G, Macdonald RG (2015) Determination of the rate constants for the NH<sub>2</sub>(X<sup>2</sup>B<sub>1</sub>) + NH<sub>2</sub>(X<sup>2</sup>B<sub>1</sub>) and NH<sub>2</sub>(X<sup>2</sup>B<sub>1</sub>) + H recombination reactions in N<sub>2</sub> as a function of temperature and pressure. *J Phys Chem A* 119:7593–7610. <https://doi.org/10.1021/acs.jpca.5b00917>
34. Goos E, Burcat A, Ruscic B (2006) Extended third millenium ideal gas and condensed phase thermochemical database for combustion with updates from active thermochemical tables. <http://garfield.chem.elte.hu/Burcat/THERM.DAT> (accessed June 6, 2024)
35. Andersen JA, van'tVeerChristensenØstbergBogaertsJensen KJMMAAD (2023) Ammonia decomposition in a dielectric barrier discharge plasma: insights from experiments and kinetic modeling. *Chem Eng Sci* 271:118550 <https://doi.org/10.1016/j.ces.2023.118550>
36. van Gessel B, Brandenburg R, Bruggeman P (2013) Electron properties and air mixing in radio frequency driven argon plasma jets at atmospheric pressure. *Appl Phys Lett* 103:064103. <https://doi.org/10.1063/1.4817936>
37. Jiang J, Bruggeman PJ (2021) Absolute ion density measurements in the afterglow of a radiofrequency atmospheric pressure plasma jet. *J Phys D: Appl Phys* 54:15LT01. <https://doi.org/10.1088/1361-6463/abd91>
38. von Keudell A, der Gathen VS (2017) Foundations of low-temperature plasma physics—an introduction. *Plasma Sources Sci Technol* 26:113001. <https://doi.org/10.1088/1361-6595/aa8d4c>
39. Bruggeman PJ, Iza F, Brandenburg R (2017) Foundations of atmospheric pressure non-equilibrium plasmas. *Plasma Sources Sci Technol* 26:123002. <https://doi.org/10.1088/1361-6595/aa97af>
40. Hsu DD, Graves DB (2005) Microhollow Cathode Discharge Reactor Chemistry. *Plasma Chem Plasma Process* 25:1–17. <https://doi.org/10.1007/s11090-004-8831-8>
41. Wang L, Zhao Y, Liu C, Gong W, Guo H (2013) Plasma driven ammonia decomposition on a Fe-catalyst: eliminating surface nitrogen poisoning. *Chem Commun* 49:3787–3789. <https://doi.org/10.1039/C3CC41301B>
42. Wang N, Otor HO, Rivera-Castro G, Hicks JC (2024) Plasma Catalysis for Hydrogen Production: A Bright Future for Decarbonization. *ACS Catal* 14(9):6749–6798. <https://doi.org/10.1021/acscatal.3c05434>

**Publisher's Note** Springer Nature remains neutral with regard to jurisdictional claims in published maps and institutional affiliations.

Springer Nature or its licensor (e.g. a society or other partner) holds exclusive rights to this article under a publishing agreement with the author(s) or other rightsholder(s); author self-archiving of the accepted manuscript version of this article is solely governed by the terms of such publishing agreement and applicable law.